



Eltes, F., Villarreal-Garcia, G. E., Caimi, D., Siegwart, H., Gentile, A. A., Hart, A. S., Stark, P., Marshall, G. D., Thompson, M. G., Barreto, J., Fompeyrine, J., & Abel, S. (2020). An integrated optical modulator operating at cryogenic temperatures. *Nature Materials*, 19, 1164-1168. <https://doi.org/10.1038/s41563-020-0725-5>

Peer reviewed version

Link to published version (if available):
[10.1038/s41563-020-0725-5](https://doi.org/10.1038/s41563-020-0725-5)

[Link to publication record in Explore Bristol Research](#)
PDF-document

This is the author accepted manuscript (AAM). The final published version (version of record) is available online via Nature Research at <https://www.nature.com/articles/s41563-020-0725-5>. Please refer to any applicable terms of use of the publisher.

University of Bristol - Explore Bristol Research

General rights

This document is made available in accordance with publisher policies. Please cite only the published version using the reference above. Full terms of use are available: <http://www.bristol.ac.uk/red/research-policy/pure/user-guides/ebr-terms/>

An integrated optical modulator operating at cryogenic temperatures

Authors: Felix Eltes^{1,3}, Gerardo E. Villarreal-Garcia², Daniele Caimi¹, Heinz Siegart¹, Antonio A. Gentile², Andy Hart², Pascal Stark¹, Graham D. Marshall², Mark G. Thompson², Jorge Barreto², Jean Fompeyrine^{1,3}, Stefan Abel^{1,3}

¹ IBM Research – Zurich, Säumerstrasse 4, 8803 Rüschlikon, Switzerland

² Quantum Engineering Technology Labs, H. H. Wills Physics Laboratory, University of Bristol, Bristol, BS8 1TL, United Kingdom

³ Lumiphase AG, Brinerstrasse 21, 8003 Zürich, Switzerland (*current affiliation*)

Integrated photonic circuits (PICs) operating at cryogenic temperatures are fundamental building blocks required to achieve scalable quantum computing, and cryogenic computing technologies^{1,2}. Silicon PICs have matured for room temperature applications, but their cryogenic performance is limited by the absence of efficient low temperature electro-optic (EO) modulation. Here we demonstrate EO switching and modulation from room temperature down to 4 K by using the Pockels effect in integrated barium titanate (BaTiO₃)-based devices³. We investigate the temperature-dependence of the nonlinear optical (NLO) properties of BaTiO₃, showing an effective Pockels coefficient of 200 pm/V at 4 K. The fabricated devices exhibit an EO bandwidth of 30 GHz, ultra-low-power tuning which is 10⁹ times more efficient than thermal tuning, and high-speed data modulation at 20 Gbps. Our results demonstrate a missing component for cryogenic PICs. Our results remove major roadblocks for the realisation of cryogenic-compatible systems in the field of quantum computing, supercomputing and sensing, and for interfacing those systems with instrumentation at room-temperature.

Cryogenic technologies are becoming essential for future computing systems, a trend fuelled by the world-wide quest to develop quantum computing systems and future generations of high-performance classical computing systems^{4,5}. While most computing architectures rely solely on electronic circuits, photonic components are becoming increasingly important (Supplementary Note, SN 1). First, PICs can be used for quantum computing approaches where the quantum nature of photons is exploited as qubits^{1,2}. Second, optical interconnects can overcome limitations in

30 bandwidth and heat leakage that are present in conventional electrical interconnect solutions for
31 digital data transfer between cryogenic processors and the room temperature environment⁶ (SN 2).
32 In addition, due to their low interaction with the environment, photons are the only viable carriers
33 to transport quantum states over large distances. Optical interfaces are therefore essential for true
34 quantum communication, necessary to connect multiple quantum computers^{7,8} and for secure
35 remote operation of quantum computers⁹. Recently, integrated photonics have also been exploited
36 in quantum computing architectures based on trapped ion qubits¹⁰. The scalability of such a system
37 is directly reliant on integrated cryogenic electro-optic modulators. The need for cryogenic
38 photonics is not limited to computing systems, but covers a wide range of technical fields, such as
39 radio astronomy¹¹, particle physics¹², and THz sensing¹³.

40 Today, the realisation of such photonic concepts is hindered by the lack of switches and modulators
41 that operate at cryogenic temperatures with low-loss, high bandwidth, and low static power
42 consumption. So far, only two concepts for cryogenic EO switches have been investigated, based
43 either on the thermo-optic effect¹⁴ or the plasma-dispersion effect¹⁵. Both mechanisms have
44 physical limitations which intrinsically restrict the low-temperature performance of such devices.
45 Thermo-optic phase shifters exploit Joule heating with large static power consumption and exhibit
46 a bandwidth of less than a few MHz¹⁶. Plasma-dispersion-based devices require very high doping
47 levels to compensate for carrier freeze-out at cryogenic temperatures and are intrinsically
48 incapable of pure phase modulation. The high doping leads to large propagation losses and devices
49 are limited to a bandwidth of <5 GHz in micro-disk modulators¹⁵. Both of these technologies are
50 fundamentally limited from providing low-loss, low-power, high-speed switching and tuning as is
51 fundamentally required for e.g. photonic quantum computing^{1,17}. InP-on-Si modulators have also
52 been explored for cryogenic use¹⁸ but with limited performance and only to temperatures of 77 K,
53 not reaching the few K or below as required by cryogenic applications.

54 The use of EO switches based on the Pockels effect has been shown to offer low propagation losses
55 and high-bandwidth, combined with low static power consumption at room temperature^{3,19–21}.
56 While the Pockels effect has no intrinsic physical limitations for use at cryogenic temperature²²,
57 making a Pockels devices requires an integrated material which retains a large Pockels coefficient
58 and which does not suffer from additional spurious effects at low temperature. No integrated
59 cryogenic Pockels modulator has previously been reported, but room temperature devices have

60 recently been demonstrated using organics²³, $\text{PbZr}_x\text{Ti}_{1-x}\text{O}_3$ ¹⁹, LiNbO_3 ²⁰, and BaTiO_3 ³. Among
61 them, BaTiO_3 stands out due to having the largest Pockels coefficients³ and exhibiting
62 compatibility with advanced silicon photonics platforms²⁴. We complete this triumvirate by
63 demonstrating that BaTiO_3 is also an ideal candidate for cryogenic EO integration.

64 Both the NLO properties and structural behaviour of BaTiO_3 thin-films are entirely unknown at
65 temperatures below 300 K. In fact, even in bulk BaTiO_3 crystals the NLO behaviour below 270 K
66 is not known, and the room temperature NLO behaviour of BaTiO_3 thin-films has only recently
67 been thoroughly investigated³. The phase transitions of thin-films are expected to differ from bulk
68 crystals²⁵ due to the structural mismatch and thermal stress that exists between the substrate and
69 the BaTiO_3 layer^{26,27}. They are entirely unknown for BaTiO_3 on Si. Predictions of the Pockels
70 tensor at cryogenic temperatures based on data at higher temperatures is not possible because in
71 complex oxide materials the functional properties can change drastically with temperature. Here,
72 we determine the cryogenic behaviour of BaTiO_3 thin films by analysing the performance of
73 BaTiO_3 -based EO switches at temperatures down to 4 K. Our results show that efficient EO
74 switching at cryogenic temperature is indeed possible and with bandwidths beyond 30 GHz. We
75 also demonstrate the applicability of such devices for low-power switching and tuning as well as
76 high-speed data modulation at 20 Gbps at 4 K.

77 In this work, we use two waveguide designs (Figure 1a) fabricated on single crystalline BaTiO_3
78 layers bonded to SiO_2 -buffered silicon substrates (see Methods). In the first design, silicon nitride
79 (SiN)-based waveguides (Figure 1d) allowed us to study the pure NLO properties of BaTiO_3 in
80 absence of mobile charge carriers which could result in an additional, non-Pockels EO response.
81 In the second, silicon (Si) waveguides served as more efficient devices (Figure 1e) to demonstrate
82 high-speed data modulation. The enhanced efficiency originates from a larger optical-mode
83 overlap with the BaTiO_3 layer (41 %, Figure 1c) than with the SiN waveguides (18 %, Figure 1b).
84 We found that the propagation losses (5.6 dB/cm, SiN device) were not affected by the presence
85 of BaTiO_3 in the active section (SN 3) throughout the temperature range studied.

86 To characterise the NLO behaviour of BaTiO_3 at 4 K, we measured the induced resonance shift in
87 a racetrack resonator as a function of the DC bias (Figure 1f), from which we determined the
88 refractive index change of BaTiO_3 (Δn_{BTO}) as a function of the applied electric field (see Methods).
89 This dependence allows us to study two of the three expected features of Pockels-based switching³:

90 NLO hysteresis and angular anisotropy, the third being the persistence of the Pockels effect at high
91 frequencies (>10 GHz)³.

92 The NLO response with a hysteretic behaviour (Figure 2a) indicates that a non-vanishing Pockels
93 effect is preserved in BaTiO₃ down to a temperature of 4 K. We determine the effective Pockels
94 coefficient, r_{eff} , by analysing the hysteretic behaviour of the refractive index change (SN 4). The
95 dependence of r_{eff} on device orientation (Figure 2b) reveals the second signature of the Pockels
96 effect, its anisotropy. The reduced magnitude at 4 K compared to room temperature is due to a
97 temperature dependence of the Pockels effect, as discussed below. While r_{eff} is reduced with
98 temperature, the EO response is expected to be present at high frequencies also at low temperature.
99 Indeed, we observe a constant EO response in racetrack resonators with a low Q factor ($Q \sim 1,800$)
100 up to 30 GHz (Figure 2b). This constitutes the highest bandwidth for any cryogenic modulator
101 reported to date. The frequency response is expected to remain flat at even higher frequency but
102 could not be measured in our experiment (see Methods). The hysteretic behaviour, anisotropy, and
103 high-speed response prove the presence of the Pockels effect in BaTiO₃ at 4 K.

104 We performed electrical characterisation of the material at low temperature using dedicated
105 electrical test structures (SN 5). The resistivity of BaTiO₃ at 4 K is very high, $>10^9$ Ωm . In fact,
106 the measured current is dominated by capacitive charging and ferroelectric switching currents
107 (Figure 2d). The field-dependent capacitance shows clear hysteretic characteristics (Figure 2e),
108 consistent with ferroelectric domain switching.

109 The measured r_{eff} at 4 K is lower than at room temperature (Figure 2b), which has two causes.
110 First, the Pockels effect itself is generally temperature dependent due to changes in strain and
111 polarisation of the crystal²⁸. Second, the non-zero elements of the Pockels tensor depend on the
112 crystal symmetry, which can change abruptly with temperature due to structural phase transitions.
113 BaTiO₃ bulk crystals are known to transition from a tetragonal phase at room temperature to
114 orthorhombic and rhombohedral phases at lower temperatures (~ 270 K and ~ 200 K
115 respectively)²⁵. Such transitions change the elements of the Pockels tensor and modify the
116 magnitude of the effective Pockels coefficients²⁸. Because phase transitions of thin-film materials
117 can be drastically affected by substrate strain^{26,27,29}, studying the properties of thin-film BaTiO₃
118 becomes critical when considering cryogenic applications. To investigate the effects of possible
119 phase transitions, we measured r_{eff} in a range from 4 to 340 K. Indeed, the magnitude of r_{eff} is

120 strongly temperature-dependent (Figure 3). A peak around 240 K, with $r_{\text{eff}} > 700$ pm/V, is
121 consistent with the reported divergence of the r_{42} element of the Pockels tensor close to the
122 tetragonal-orthorhombic transition²⁸. Consistently, the permittivity of the BaTiO₃ layer (see
123 Methods) also shows a peak in the same temperature range (SN 6), confirming that the abrupt
124 change in r_{eff} is caused by a phase transition. Below 240 K the magnitude of r_{eff} decreases gradually
125 to around 200 pm/V at 4 K. In addition to the phase transition at 240 K, a second phase transition
126 occurs above 100 K causing a rapid change in r_{eff} of 90° devices. This phase transition is also
127 observed in the qualitative behaviour of the NLO hysteresis which shows that the transitions is
128 induced by the electric field (SN 6). While r_{eff} of BaTiO₃ is reduced at 4 K compared to room
129 temperature, the value of ~200 pm/V is still larger than most other material systems at room
130 temperature^{19,20}. The effect of a reduced Pockels coefficient on the energy efficiency of EO
131 switching is partially compensated for by a simultaneous reduction of the permittivity of BaTiO₃
132 (SN 6). Additionally, the conductivity of BaTiO₃ is reduced by more than four orders of magnitude
133 (SN 5), resulting in a negligible static power consumption of BaTiO₃-devices in cryogenic
134 environments. No material instability or drift, as could for example be caused by pyroelectric
135 effects, were observed at cryogenic or room temperature in any experiment.

136 We have reported the first ever measurement of the cryogenic NLO properties of BaTiO₃, and
137 indeed of any oxide thin-film material. The methods used to characterize these properties will
138 enable further research to improve the cryogenic performance through engineering of the material
139 properties²⁹. However, already today we can use BaTiO₃ to demonstrate cryogenic devices with
140 outstanding performance.

141 We demonstrate the applicability of BaTiO₃ for cryogenic photonic applications by two examples:
142 low-power EO switching and high-speed data modulation. For switching we use a 500 μm Mach-
143 Zehnder interferometer with 2×2 multimode interference splitters, applying a voltage to one arm.
144 Because the leakage current through BaTiO₃ at 4 K is 10⁴ times lower than at 300 K, less than
145 10 pW static power is consumed when inducing a π phase shift to switch between the two optical
146 outputs using an electric field of 6×10^6 V/m (Figure 4a,b), corresponding to a voltage of ~50 V in
147 the given device geometry ($V_{\pi}L = 5$ Vcm). Compared to state-of-the-art technology based on
148 thermo-optic phase shifters¹⁴, static tuning using BaTiO₃ is one billion times more power efficient.
149 The dynamic energy of the switch is ~30 pJ, which could be reduced to ~2 pJ, at a voltage of <5 V,

150 in an optimised device geometry (SN 7). Another important metric for EO switches is the losses
151 in the device. Based on the measured propagation losses (5.6 dB/cm) and the device geometry we
152 estimate an insertion loss of <1 dB (SN 3). The propagation losses are dominated by scattering
153 losses in the SiN waveguide which can be reduced significantly by using a state-of-the-art
154 fabrication process. SiN waveguides with propagation losses as low as 1 dB/m have been
155 reported³⁰.

156 As a second example, we performed data modulation experiments by sending a pseudo-random
157 bit-sequence to a ring modulator ($Q \sim 6'000$) fabricated with BaTiO₃-Si waveguides and recording
158 the optical eye-diagram (Figure 4c,d). Data transmission at rates up to 20 Gbps are achieved with
159 our experimental setup using a drive voltage (V_{pp}) of just 1.7 V, resulting in an extremely low
160 energy consumption of 45 fJ/bit.

161 In conclusion, we have shown that BaTiO₃ thin films can be used to realise electro-optic switches
162 and modulators for efficient cryogenic operation of silicon photonic integrated circuits. We have
163 demonstrated low-power switching, as well as high-speed data modulation. Combining BaTiO₃
164 with silicon photonic integrated circuits, we make a building block available that was previously
165 inaccessible for any cryogenic circuits. We anticipate that these components are a milestone for a
166 versatile platform of cryogenic photonics for applications as diverse as quantum computing and
167 communication^{1,8}, astronomy¹¹, fundamental physics¹², and cryogenic sensing concepts¹³.

168

- 169 1. Silverstone, J. W., Bonneau, D., O'Brien, J. L. & Thompson, M. G. Silicon quantum
170 photonics. *IEEE J. Sel. Top. Quantum Electron.* **22**, 6700113 (2016).
- 171 2. O'Brien, J. L., Furusawa, A. & Vučković, J. Photonic quantum technologies. *Nat. Photonics*
172 **3**, 687–695 (2009).
- 173 3. Abel, S. *et al.* Large Pockels effect in micro- and nanostructured barium titanate integrated
174 on silicon. *Nat. Mater.* **18**, 42–47 (2019).
- 175 4. Mukhanov, O. A. Energy-Efficient single flux quantum technology. *IEEE Trans. Appl.*
176 *Supercond.* **21**, 760–769 (2011).
- 177 5. Ladd, T. D. *et al.* Quantum Computing. *Nature* **464**, 45–53 (2010).
- 178 6. Zeghbroeck, B. Van. Optical data communication between Josephson-junction circuits and
179 room-temperature electronics. *IEEE Trans. Appl. Supercond.* **3**, 2881–2884 (1993).
- 180 7. Kimble, H. J. The quantum internet. *Nature* **453**, 1023 (2008).
- 181 8. Javerzac-Galy, C. *et al.* On-chip microwave-to-optical quantum coherent converter based on
182 a superconducting resonator coupled to an electro-optic microresonator. *Phys. Rev. A* **94**,
183 053815 (2016).
- 184 9. Greganti, C., Roehsner, M. C., Barz, S., Morimae, T. & Walther, P. Demonstration of
185 measurement-only blind quantum computing. *New J. Phys.* **18**, 303–309 (2016).
- 186 10. Mehta, K. K. *et al.* Integrated optical addressing of an ion qubit. *Nat. Nanotechnol.* **11**, 1066
187 (2016).
- 188 11. Johnston, A. R. *et al.* Optical links for cryogenic focal plane array readout. *Opt. Eng.* **33**,
189 2013–2019 (1994).
- 190 12. Dowell, J. D. *et al.* Optoelectronic analogue signal transfer for LHC detectors. in
191 *CERN/DRDC 91-41* (1991).
- 192 13. Benea-Chelmus, I.-C., Settembrini, F. F., Scalari, G. & Faist, J. Electric field correlation
193 measurements on the electromagnetic vacuum state. *Nature* **568**, 202–206 (2019).
- 194 14. Elshaari, A. W., Zadeh, I. E., Jöns, K. D. & Zwiller, V. Thermo-Optic Characterization of
195 Silicon Nitride Resonators for Cryogenic Photonic Circuits. *IEEE Photonics J.* **8**, (2016).
- 196 15. Gehl, M. *et al.* Operation of high-speed silicon photonic micro-disk modulators at cryogenic
197 temperatures. *Optica* **4**, 374 (2017).
- 198 16. Harris, N. C. *et al.* Efficient, Compact and Low Loss Thermo-Optic Phase Shifter in Silicon.
199 *Opt. Express* **22**, 83–85 (2014).
- 200 17. Li, Y., Humphreys, P. C., Mendoza, G. J. & Benjamin, S. C. Resource Costs for Fault-
201 Tolerant Linear Optical Quantum Computing. *Phys. Rev. X* **5**, 41007 (2015).
- 202 18. Pintus, P. *et al.* Characterization of heterogeneous InP-on-Si optical modulators operating
203 between 77 K and room temperature. *APL Photonics* **4**, 100805 (2019).

- 204 19. Alexander, K. *et al.* Nanophotonic Pockels modulators on a silicon nitride platform. *Nat.*
205 *Commun.* **9**, 3444 (2018).
- 206 20. Wang, C. *et al.* Integrated lithium niobate electro-optic modulators operating at CMOS-
207 compatible voltages. *Nature* **562**, 101–104 (2018).
- 208 21. Eltes, F. *et al.* Low-loss BaTiO₃-Si waveguides for nonlinear integrated photonics. *ACS*
209 *Photonics* **3**, 1698–1703 (2016).
- 210 22. Herzog, C., Poberaj, G. & Günter, P. Electro-optic behavior of lithium niobate at cryogenic
211 temperatures. *Opt. Commun.* **281**, 793–796 (2008).
- 212 23. Lauermann, M. *et al.* 40 GBd 16QAM Signaling at 160 Gb/s in a Silicon-Organic Hybrid
213 Modulator. *J. Light. Technol.* **33**, 1210–1216 (2015).
- 214 24. Eltes, F. *et al.* A BaTiO₃-based electro-optic Pockels modulator monolithically integrated on
215 an advanced silicon photonics platform. *J. Light. Technol.* **37**, 1456–1462 (2019).
- 216 25. Kay, H. F. & Vousden, P. XCV. Symmetry changes in barium titanate at low temperatures
217 and their relation to its ferroelectric properties. *Lond. Edinb. Dublin Philos. Mag. J. Sci.* **40**,
218 1019–1040 (1949).
- 219 26. He, F. & Wells, B. O. Lattice strain in epitaxial BaTiO₃ thin films. *Appl. Phys. Lett.* **88**,
220 152908 (2006).
- 221 27. Tenne, D. A. *et al.* Absence of low-temperature phase transitions in epitaxial BaTiO₃ thin
222 films. *Phys. Rev. B - Condens. Matter Mater. Phys.* **69**, 2–6 (2004).
- 223 28. Bernasconi, P., Zgonik, M. & Gunter, P. Temperature dependence and dispersion of electro-
224 optic and elasto-optic effect in perovskite crystals. *J. Appl. Phys.* **78**, 2651–2658 (1995).
- 225 29. Acosta, M. *et al.* BaTiO₃-based piezoelectrics: Fundamentals, current status, and
226 perspectives. *Appl. Phys. Rev.* **4**, (2017).
- 227 30. Pfeiffer, M. H. P. *et al.* Ultra-smooth silicon nitride waveguides based on the Damascene
228 reflow process: fabrication and loss origins. *Optica* **5**, 884–892 (2018).

229

230
231
232
233
234
235
236
237

238

239
240

241

242
243

244

245
246
247
248
249
250
251
252
253

Acknowledgements

This work has received funding from the European Commission under grant agreements no. H2020-ICT-2015-25- 688579 (PHRESCO) and H2020-ICT-2017-1-780997 (plaCMOS), from the Swiss State Secretariat for Education, Research and Innovation under contract no. 15.0285 and 16.0001, from the Swiss National Foundation project no 200021_159565 PADOMO, from EPSRC grants EP/L024020/1, EP/M013472/1, and EP/K033085/1, the UK EPSRC grant QuPIC (EP/N015126/1), and ERC grant 2014- STG 640079. JB thanks Dr. Döndü Sahin for her assistance with the experimental setup.

Competing interests

F.E., J.F., and S.A. are involved in developing barium titanate technologies at Lumiphase AG. M.G.T. is involved in developing photonic quantum technologies at PsiQuantum Corporation.

Data availability

The data that support the findings of this study are available from the corresponding authors upon reasonable request.

Author contributions

F.E. and J.F. fabricated and structurally characterised the epitaxial BaTiO₃/SrTiO₃ layer stack with support from H.S.. F.E designed all photonic circuits and fabricated them with support from D.C.. F.E., P.S. and S.A. performed optical simulations for the device design. G.E.V-G., F.E., A.A.G., A.H., G.D.M. and J.B. characterised the EO performance at different temperatures including low-speed and RF measurements. The EO data was analysed by F.E. and A.A.G.. F.E. and P.S. performed all electrical measurements. The concept for this work was defined by S.A., G.D.M. and M.G.T. and implemented by F.E. with support of S.A. and J.B.. F.E., J.F., and S.A. wrote the manuscript with contributions from all authors.

Methods

254

255 **Device design and fabrication.** Single crystalline BaTiO₃ was deposited on top of an epitaxial 4-
256 nm-thick SrTiO₃ seed layer by molecular beam epitaxy on 8” silicon-on-insulator (SOI) wafers
257 with 220-nm-thick device silicon layer for SiN-based devices, and on 2” SOI wafers with 100-nm-
258 thick device silicon for Si-based devices, following a process described elsewhere³. Direct wafer
259 bonding was used to transfer the BaTiO₃ and device Si layers onto high-resistivity Si wafers
260 capped with a 3- μ m-thick thermal oxide. Specifics of the direct wafer bonding process can be
261 found in ref. ³.

262 For SiN-based waveguides the device Si layer was removed by dry etching, followed by chemical
263 vapor deposition of SiN. The waveguide layer (Si or SiN) was patterned by dry etching. After
264 waveguide patterning, a combination of SiO₂ cladding deposition, via etching, and metallisation
265 was used to form the final cross-section. Intermediate annealing steps at 400°C under O₂
266 atmosphere were used to reduce propagation losses²¹.

267 The SiN-based waveguides use an 80-nm-thick BaTiO₃ layer, and 150-nm-thick SiN layer. The
268 strip-waveguide width is 1.1 μ m. The SiN thickness and waveguide width were chosen to ensure
269 guiding of a single TE mode, and to maximize the overlap of that mode with the BaTiO₃ layer.
270 The electrode-to-electrode gap is 9 μ m to ensure no added losses caused by metal absorption. The
271 racetrack resonators have a bend radius of 50 μ m and straight sections of 75 μ m length. The
272 coupling gap (0.53 μ m) between the access waveguide and the resonator was optimized for critical
273 coupling.

274 The Si strip-waveguides were fabricated using 225-nm-thick BaTiO₃ and 100-nm-thick Si. The
275 waveguide width is 0.75 μ m. As for the SiN-based waveguides the waveguide dimension,
276 including the Si thickness, were designed for TE single mode operation, with an optimized optical
277 overlap with the 225-nm-thick BaTiO₃ layer. The racetrack resonator that was used has a bending
278 radius of 15 μ m and straight sections of 30 μ m, and the electrode-to-electrode gap is 2.3 μ m. The
279 small electrode gap causes additional propagation losses in the resonator ensuring a Q-factor
280 allowing >30 GHz bandwidth. The coupling gap of ~0.1 μ m was optimized for critical coupling.

281 **Cryogenic measurements.** The cryogenic electro-optic measurements were performed in a
282 Lakeshore CPX cryogenic probe station, fitted with RF (40 GHz BW, K-type connectors) and

283 optical feedthroughs. DC and RF signals were applied to the devices using RF probes, and optical
284 coupling was achieved using a fibre array with polarisation maintaining fibres for 1550 nm. A
285 tuneable laser (EXFO T100S-HP) and power meter were used to record transmission spectra
286 (EXFO CT440). The cryogenic electrical measurements were performed in a Janis cryogenic probe
287 station equipped with DC probes. Current-voltage and capacitance-voltage measurements were
288 performed using a parameter analyser. Both cryogenic probe stations were cooled by liquid helium
289 to a base temperature of 4.2 K.

290 **DC EO characterisation.** The DC electro-optic response was extracted by applying a voltage to
291 the electrodes of a racetrack resonator and measuring the shift in resonance wavelength ($\Delta\lambda$),
292 compared to the unbiased case, as a function of the applied voltage. From the measured wavelength
293 shift, the change in BaTiO₃ refractive index (Δn_{BTO}) can be estimated as

$$294 \quad \Delta n_{\text{BTO}} = \frac{\lambda_0 \cdot \Delta\lambda}{FSR \cdot L_E \cdot \Gamma_{\text{BTO}}}$$

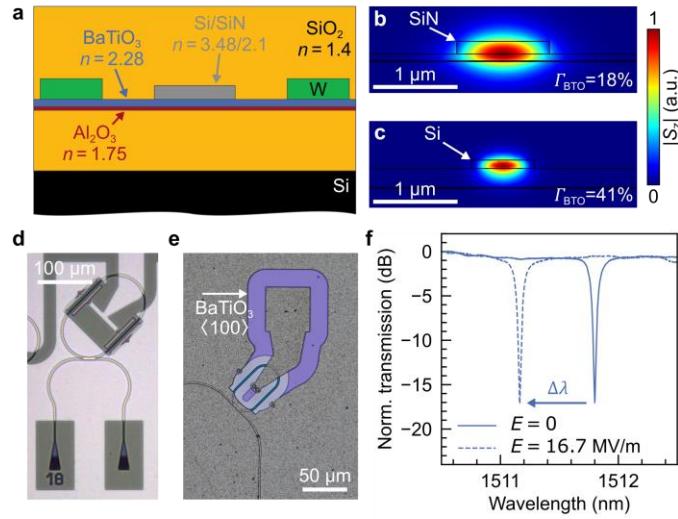
295 where Γ_{BTO} is the optical confinement in BaTiO₃, FSR is the free spectral range of the resonator,
296 L_E is the electrode length, and λ_0 is the resonance wavelength with no voltage.³ The effective
297 Pockels coefficient, r_{eff} , was then determined according to the procedure described in SN 4.

298 **RF frequency response.** To measure the EO frequency response (EO S_{21}) a vector network
299 analyser (VNA, Keysight PNA 50 GHz) was used to apply the electrical stimulus to a BaTiO₃ ring
300 modulator. The modulated optical signal was applied to a photodiode (Newport 1024) and the
301 response recorded by the VNA. Electrical calibration was performed before the measurement, and
302 the response of the photodetector was compensated for the data analysis. While the VNA could
303 generate signals up to 50 GHz, the bandwidth of the photodetector was 26 GHz, which in
304 combination with large frequency-dependent electrical losses in the cryogenic probe station (SN 8)
305 makes it impossible to measure the bandwidth beyond 30 GHz.

306 **Data modulation experiments.** For the data modulation experiment, a racetrack resonator
307 modulator with a Si strip-waveguide was used. The electrical signal was generated using an
308 arbitrary waveform generator. A pseudo-random bit stream of 2^7-1 bits was used for modulation.
309 The electrical signal was pre-distorted to compensate for the finite time-response of the electrical
310 signal path (SN 8). The signal was amplified using a RF amplifier and sent to the cryogenic setup,
311 with an estimated voltage swing on the device of 1.7 V (SN 8). A Pritel FA-23 EDFA was used to

312 amplify the modulated optical signal which was applied to a photo diode and recorded on an
313 oscilloscope.

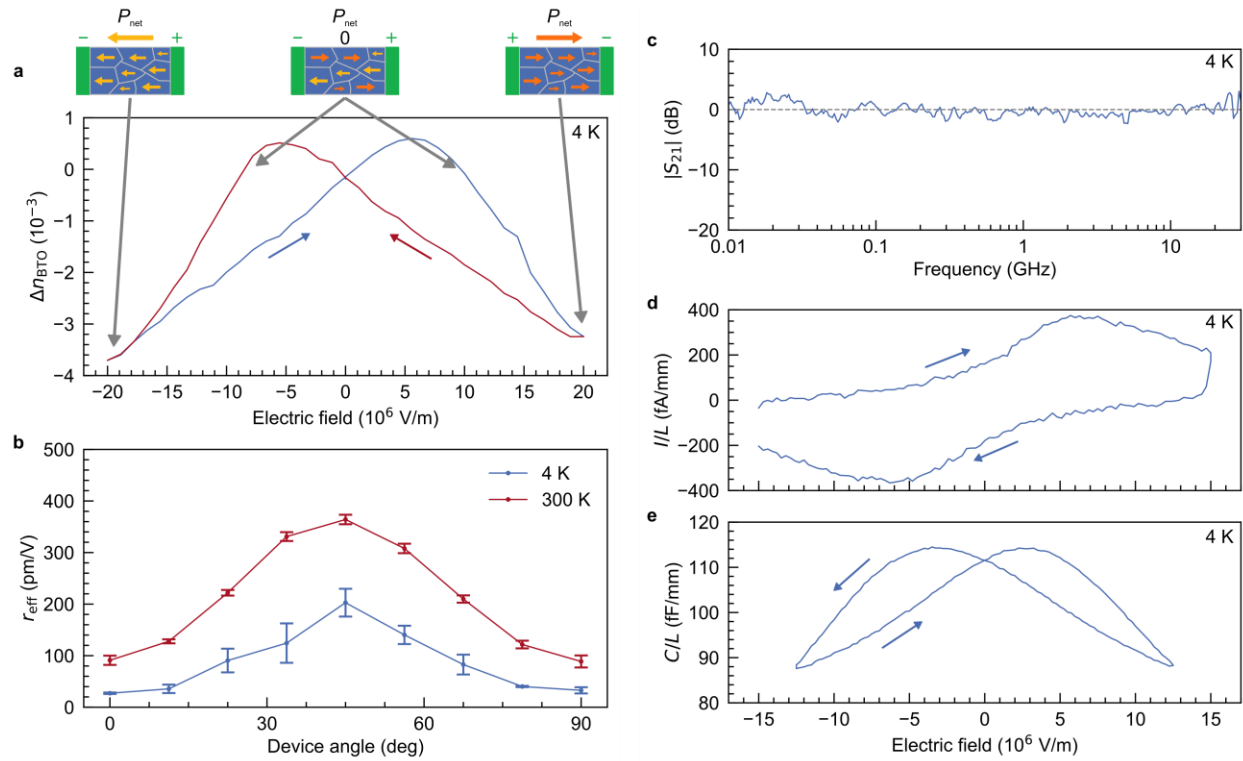
314



315

316 **Figure 1. BaTiO₃ electro-optic device concept.** **a**, Schematic cross-section of the devices. A silicon or silicon nitride layer forms a strip-waveguide
 317 (grey) on top of an BaTiO₃ layer (blue). A thin Al₂O₃ layer (red) was used to improve adhesion (Methods). Lateral electrodes fabricated with W
 318 (green) are used to apply an electric field across the BaTiO₃. The devices are embedded in SiO₂ (yellow) layers on top of silicon substrates (black).
 319 The refractive indices of BaTiO₃ and SiN were measured using spectroscopic ellipsometry. **b**, **c**, Simulations of the Pointing vector, $|S_z|$, of the
 320 transverse electric (TE) mode of the SiN waveguide geometry and the Si waveguide geometry, respectively. The two waveguide geometries show
 321 an optical confinement in BaTiO₃, Γ_{BTO} , of 18 % and 41 %, respectively. **d**, **e**, Optical micrographs of BaTiO₃-SiN and BaTiO₃-Si racetrack
 322 resonators, respectively, used to characterise BaTiO₃ and demonstrate device functionality. The phase shifter section is embedded in the resonator
 323 which is evanescently coupled to access waveguides. The signal electrodes are connected to pads and the ground electrodes to a ground plane, for
 324 contacting using electrical probes. **f**, Characterisation principle of resonant electro-optic switches, showing example data of the shift in resonance
 325 wavelength between no applied field (solid line) and 16.7 MV/m (dashed line), which in this device corresponds to 150 V resulting in a shift of 4.3
 326 pm/V. The shift in resonance wavelength, $\Delta\lambda$, is measured for an applied electric field and converted to the material properties of BaTiO₃ (see
 327 Methods).

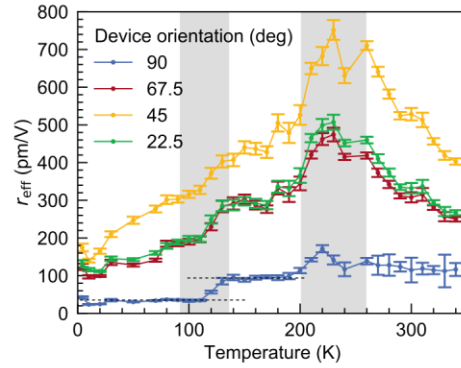
328



329

330 **Figure 2. Electro-optic and electrical response of BaTiO₃-based optical switches at 4 K.** a, Refractive index change of BaTiO₃ as a function of
 331 applied electric field for a device in the 11.25° direction (as defined in b). The hysteretic behaviour between increasing (blue) and decreasing (red)
 332 voltage originates from ferroelectric domain switching in the BaTiO₃, as illustrated schematically on top. P_{net} is the net polarization of all the
 333 domains. The arrows indicate the polarization of individual ferroelectric domains (blue) when a field is applied to lateral electrodes (green). b,
 334 Angular anisotropy of the effective Pockels coefficient in BaTiO₃ measured at 4 K and 300 K. The angle is defined relative to the BaTiO₃<100>
 335 direction. The same anisotropy as for BaTiO₃ at room temperature is observed but with reduced magnitude. The error bars show the combined
 336 standard error of the fit and from averaging measurements of multiple devices with the same orientation. c, Electro-optic S_{21} -parameter of BaTiO₃
 337 ring resonator showing a flat response up to a frequency of 30 GHz at 4 K. The dashed line indicates 0 dB as a guide to the eye. d, Current measured
 338 as a function of electric field across the BaTiO₃ layer showing extremely low current flowing through the material. The current is dominated by
 339 capacitive charging, causing the offset between the sweep directions (indicated by the arrows), together with ferroelectric switching current resulting
 340 in the observed peaks (SN 5). e, Capacitance as a function of electric field, showing characteristic ferroelectric hysteresis and field-dependent
 341 permittivity.

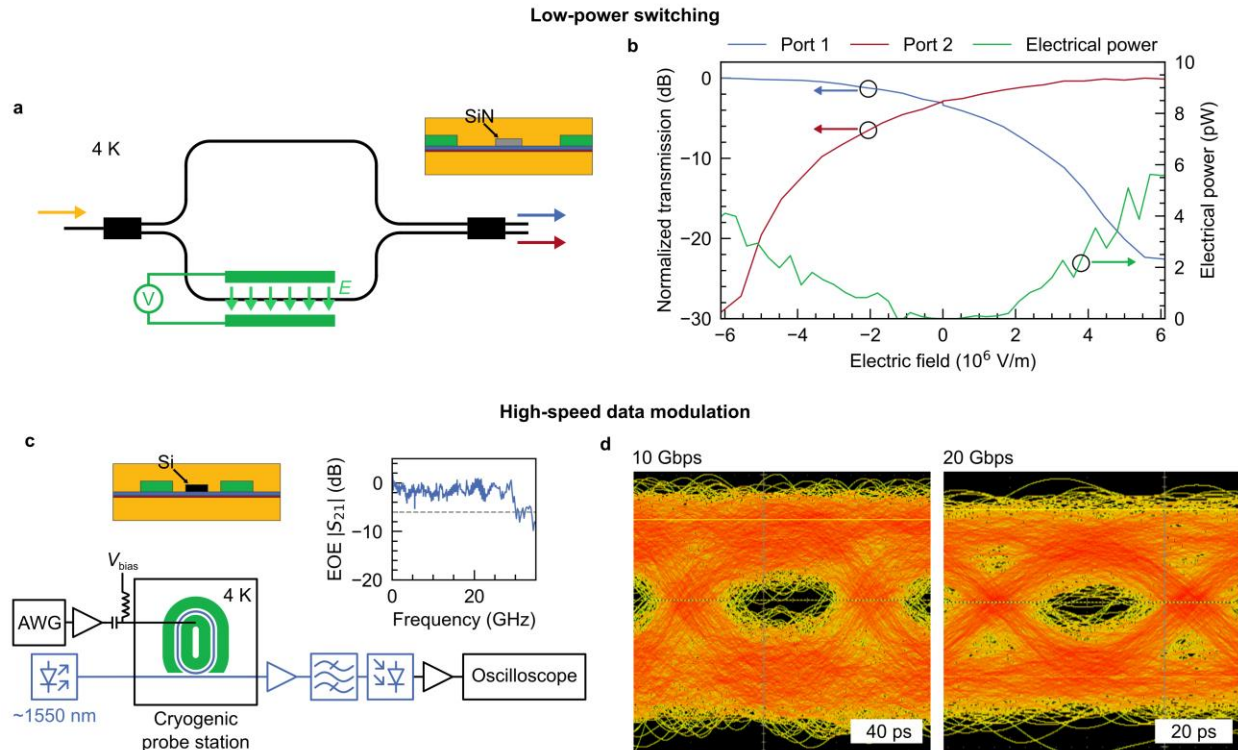
342



343

344 **Figure 3. Temperature dependence of the Pockels effect in BaTiO₃.** The effective Pockels coefficient along different crystal orientations at
 345 temperatures from 4 K to 340 K. The peak around 240 K is the signature of a phase transition in BaTiO₃. A second, field-induced phase transition
 346 occurs around 100 K, causing a sharp drop of r_{eff} in 90° devices (indicated by horizontal dashed lines). This phase transition is also evident in the
 347 qualitative evaluation of the optical response (SN 6). The grey areas indicate the temperature ranges of the respective phase transitions. The error
 348 bars show the standard error of the fit used to extract the Pockels coefficients (SN 4).

349



350

351 **Figure 4. Demonstration of low-power switching and high-speed data modulation with BaTiO₃-based devices at 4 K.** **a**, Schematic of Mach-
 352 Zehnder (MZ) configuration used to switch between two ports. The yellow arrow indicates the input port and the red and blue arrows indicate
 353 output ports 1 and 2, respectively. Multi-mode interference splitters were used to split and combine the signal at the input and output ports. A
 354 voltage source, V, is used to apply an electric field, E, indicated by green arrows, across one arm of the MZ interferometer. The inset shows the
 355 waveguide cross-section. **b**, Transmission from both ports of a MZ switch as a function of applied electric field, along with the static power
 356 consumption. When fully switching between outputs, less than 10 pW static power is consumed, and only 30 pJ of dynamic energy. The field is
 357 kept below the coercive field of BaTiO₃ (SN 9) to exclude contributions from ferroelectric domain switching. **c**, Schematic of the experimental
 358 setup for data modulation. The data signal was generated using an arbitrary waveform generator (AWG) which was amplified and then combined
 359 with a bias voltage, V_{bias}, using a bias tee. A tuneable laser set to ~1550 nm provided the optical carrier. After modulation in the cryogenic
 360 probe station, the optical signal was amplified by a fibre amplifier and filtered before being detected by a photodiode. The electrical signal from the
 361 photodiode was amplified and then recorded on a real-time oscilloscope. The left inset show the waveguide cross-section and the right inset shows
 362 the electro-optic-electric (EOE) frequency response of the modulator. **d**, Eye diagrams recorded at 10 and 20 Gbps with V_{pp} = 1.7 V, corresponding
 363 to modulation energy of 45 fJ/bit. The opening of the eyes is limited by noise from amplified spontaneous emission of the amplifier used in the
 364 experiment (SN 8).